JOURNAL OF SOLID STATE CHEMISTRY **133,** 545–554 (1997)
ARTICLE NO. SC977528

New Defective Brannerite-Type Vanadates

II. Synthesis and Study of $Mn_{1-x-y}Ag_y\Phi_xV_{2-2x-y}Mo_{2x+y}O_6$ Solid Solutions: Ag–Mn-stabilized Hexagonal MoO_3

Bogna Napruszewska, Piotr Olszewski, and Jacek Ziółkowski[1]

Institute of Catalysis and Surface Chemistry, Polish Academy of Sciences, ul. Niezapominajek, 30-239 Kraków, Poland

Received January 3, 1997; in revised form June 26, 1997; accepted June 29, 1997

MnV_2O_6 (below 540°C) and $AgVMoO_6$ are monoclinic $C2/m$ brannerite-type structures. They show complete miscibility, forming $MnAg = Mn_{1-y}Ag_yV_{2-y}Mo_{1+y}O_6$ solid solutions. MnAg is able to incorporate an excess of MoO_3 and form $MnAg\Phi = Mn_{1-x-y}\Phi_xAg_yV_{2-2x-y}Mo_{2x+y}O_6$ phases (Φ = cation vacancy in the original Mn/Ag site) belonging to the pseudoternary MnV_2O_6–$AgVMoO_6$–MoO_3 system. The system can be visualized as an equilateral triangle with $X = 100x$ and $Y = 100y$ coordinates along the MnV_2O_6–MoO_3 and MnV_2O_6–$AgVMoO_6$ arms, respectively. The limit of the existence of $MnAg\Phi$ is almost linear and extends between the X–Y points $S_1 = (45, 00)$ and $S_2 = (12, 88)$. As the ionic radii of dopants (Ag^+/Mn^{2+}, Mo^{6+}/V^{5+}) are larger than those of the mother cations, the lattice constants in both series—MnAg and almost saturated $MnAg\Phi$ (located along the S_1S_2 curve—rise systematically with an increase in Y. Behind the S_1S_2 curve, saturated $MnAg\Phi$ has been observed accompanied by "hexagonal MoO_3" (h-MoO_3), Y phase = $Mn_{0.15}V_{0.3}Mo_{0.7}O_6$, by $(Mo_xV_{1-x})_2O_5$, and sometimes by orthorhombic MoO_3 and $MnMoO_4$. According to the literature, so-called h-MoO_3 is a defective tunnel structure stabilized by the inserted free or hydrated $L = K^+$, Rb^+, Cs^+, NH_4^+ ions. The formula of dry h-MoO_3 is $L_{0.13}V_{0.13}Mo_{0.87}O_3$(I). Ag was believed to be too small to stabilize the peculiar h-MnO_3. Despite that, we observed Ag-containing h-MoO_3 in the field of the MnV_2O_6–$AgVMoO_6$–MoO_3 triangle. Attempts to obtain a pure Ag-containing h-MoO_3 have failed so far; apparently the presence of Mn (beside Ag) stabilizes the h-MoO_3 structure and the formula is more complex as compared with I. The phase diagram of the MnV_2O_6–$AgVMoO_6$ system reveals great similarity to those containing Li and Na instead of Ag. All three diagrams involve a narrow lens-type solidus–liquidus gap at high Y and two peritectic meltings at lower Y, yielding, besides liquid, the high-temperature β-MnAg polymorph and $Mn_2V_2O_7$.

[1]To whom correspondence should be addressed.

1. INTRODUCTION

About 30 years ago Ruh and Wadsley (1) resolved the structure of the mineral $ThTi_2O_6$, containing some dopants. The structure, called *brannerite*, has been identified as monoclinic, $C2/m$ (although $C2$ and Cm symmetries are not excluded among the brannerite-type family, described below). In this layered AB_2O_6 structure (visualized in Fig. 1) distorted BO_6 octahedra sharing edges form the anionic sheets parallel to (001), with packing tight along [010] and loose along [100]. The edge-sharing, distorted AO_6 octahedra make isolated [010] pillars, linking the anionic layers in the [001] direction. The pillars are tight in the [001] direction and bulky along [010]. The $c \sin \beta$ parameter expresses the distance between the anionic layers of the structure.

Soon it was proved that either a number of bivalent metal vanadates $Me^{2+}V_2^{5+}O_6$ (Me = Mg, Mn, Co, Cu, Zn, Hg, Cd) adapt this structure or the structure is exhibited by at least one of their polymorphs (2–9). Further progress was made when it was reported that the same structure is possessed by compounds of formula $L^{1+}V^{5+}Mo^{6+}O_6$ (L = Li, Na, Ag) (10, 11). Finally, the structure appeared to be amenable to random isomorphous substitutions including in some cases the cation vacancies Φ in the Me/L sublattice, and the following solid solutions were identified ($X = 100x$, $Y = 100y$):

— $L\Phi = L_{1-x}\Phi_xV_{1-x}Mo_{1+x}O_6$ with $0 \le X \le 16$ for L = Li, $0 \le X \le 30$ for Na, $0 \le X \le 12$ for Ag, and $18 \le X \le 24$ for K [although pure $KVMoO_6$ (12) has never been synthesized in the brannerite form] (10).

— $Me\Phi = Me_{1-x}\Phi_xV_{2-2x}Mo_{2x}O_6$ with $0 \le X \le 45$ for Mn, and $0 \le X \le 22$ for Co, $0 \le X \le 15$ for Zn (8, 13, 14).

— $MeL = Me_{1-y}L_yV_{2-y}Mo_yO_6$ with $0 \le Y \le 100$ for Mn/Li, Mn/Na, Zn/Li, and Mg/Li and $5 \le Y \le 100$ for Co/Li, (8, 15–18).

0022-4596/97 $25.00

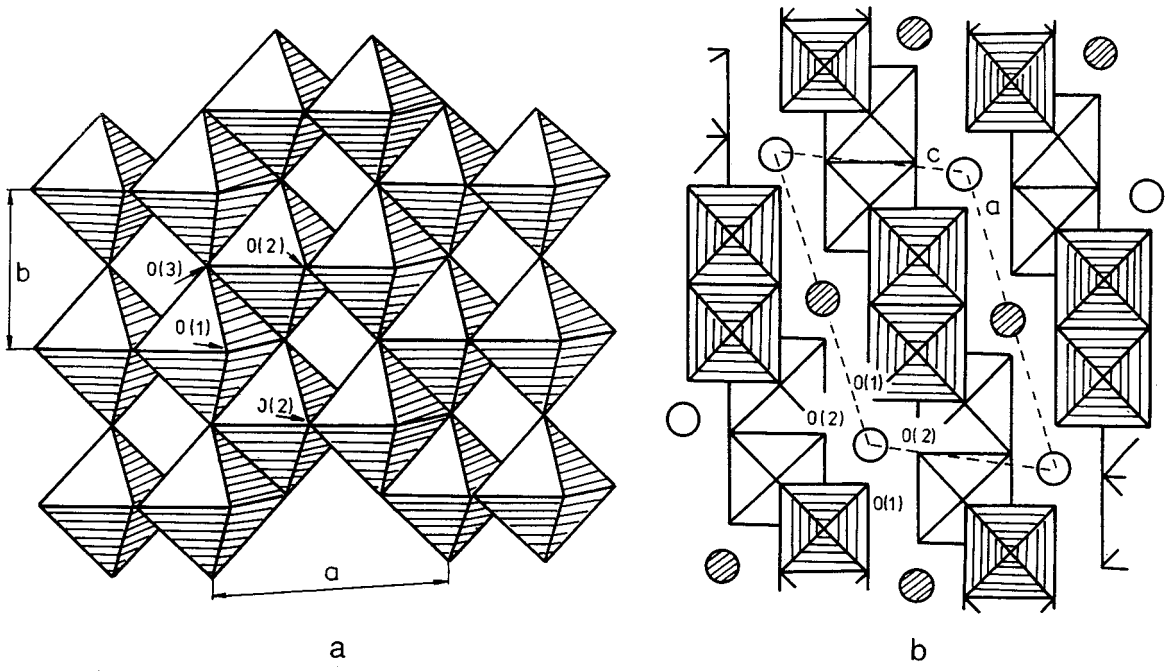

FIG. 1. Idealized outline of the brannerite-type MeV_2O_6 structure [after (1)]. (a) A sheet of VO_6 octahedra parallel to the (001) plane [nonequivalent oxygens linked with one, two, or three vanadium atoms are labeled O(1), O(2), and O(3), respectively]. (b) Projection of the structure on the (010) plane with marked *Me* cations and VO_6 groups on two different levels [0 and 0.5 of (b)].

— $MeL\Phi = Me_{1-x-y}L_y\Phi_xV_{2-2x-y}Mo_{2x+y}O_6$ (Mn/Li, Co/Li, Zn/Li, Mg/Li, Mn/Na, Cu^+/Cu^{2+} with variable X_{max} ranging up to 45 and $Y_{max} = 100$ (14–19).

It may be relevant to recall that the stoichiometry of $MeL\Phi$ may be expressed as $Me_{1-x-y}L_y\Phi_xV_{2-2x-y}Mo_{2x+y}O_6 = (1-x-y)MeV_2O_6 + yLVMoO_6 + 2xMoO_3$. $MeL\Phi$ compounds thus are pseudoternary MeV_2O_6–$LVMoO_6$–MoO_3 systems and their composition may be represented using an equilateral triangle (cf. Fig. 2) with the composition variables $X = 100x$ marked along the MeV_2O_6–MoO_3 and $LVMoO_6$–MoO_3 arms ($Me\Phi$ and $L\Phi$ solid solutions), $Y = 100y$ marked along the MeV_2O_6–$LVMoO_6$ arm (MeL solutions), and $MeL\Phi$ solutions occupying a part of the triangle area.

In view of the above brief summary of the literature data one can conclude that the layered AB_2O_6 brannerite-type structure of vanadates or vanadomolybdates is composed of the following:

i. VO_6/MoO_6 octahedra, making (001) sheets and containing ions of almost the same size. The octahedral ionic radii of V^{5+} and Mo^{6+} are 0.476 and 0.498 Å, respectively [the selected examples of radii compiled by one of the authors (20) and by Shannon (21) are gathered later in Table 5]. All these octahedra are filled with cations.

ii. AO_6 [010] pillars linking the above-mentioned sheets, which may contain either monovalent or bivalent cations or cation vacancies in variable amounts, the size of monovalent cations ranging from 0.728 (Li^+) to 1.440 (K^+) and that of bivalent cations from 0.707 (Mg^{2+}) to 1.020 Å (Hg^{2+}) (20).

iii. The stability of the structure apparently depends on the filling of the [010] pillars [strains resulting from the ion

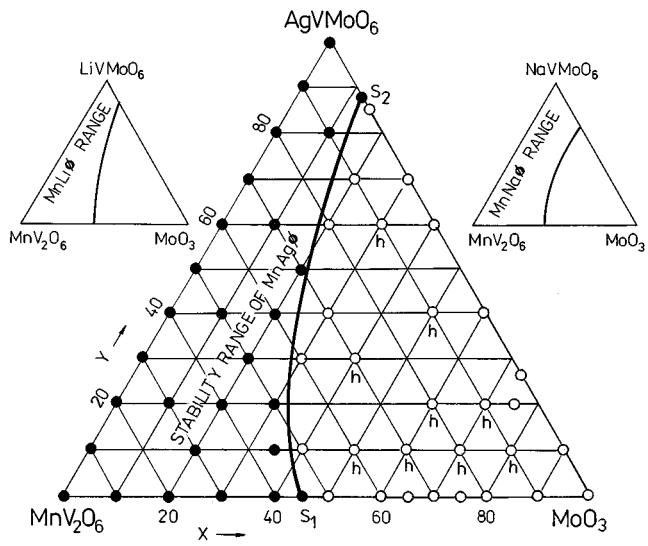

FIG. 2. Area of stability of the $MnAg\Phi$ solid solutions. Solid circles correspond to the studied samples composed of single brannerite-type phase. Open circles, behind the S_1S_2 boundary, represent studied samples contaminated with other compounds; "h" marks the samples containing Ag(Mn)-stabilized MoO_3. The stability ranges of $MnLi\Phi$ (15) and $MnNa\Phi$ (18) are recalled in the upper part of the figure.

sizes simultaneously present, and cation cavities and bond energy distribution (22) dependent on the variable amounts of Me^{2+}, L^{+}, and Φ].

The aim of our former work (8, 9, 13–19) and contemporary work has been to determine how far the brannerite-type structure is resistant to the consequences of doping indicated in point iii. Partial answers have been offered in the quoted papers. Now we intend to extend the studies on the Ag–Mn–V–Mo–O system (present work) and K–Mn–V–Mo–O system (23).

2. EXPERIMENTAL

The compositions of all samples prepared and studied by XRD and partly by DTA are indicated in Fig. 2. Samples were synthesized by the amorphous citrate method (24), adapted empirically for the present systems (15). Reactants were $AgNO_3$, $MnCO_3$, NH_4VO_3, $(NH_4)_6Mo_7O_{24}\cdot 4H_2O$, 0.1 *M* HNO_3, 0.1 *M* ammonia, and citric acid, all of p.a. grade. The procedure has been described (15). The final thermal treatment was carried out in air at 520–530°C for 24 h (or more, up to 96 h, if doubt arises whether the reaction had been completed); thereafter, the samples were quenched.

XRD patterns were obtained with a DRON-2 diffractometer using Cu$K\alpha$ radiation and in some cases with an internal standard of Al ($a = 4.0492$ Å at 25°C). Data were collected on a floppy disk and processed with the SMOK (Elector Co., Kraków, Poland) and LATCON (CERN library) programs. Reflections of $5^\circ < 2\theta < 80^\circ$ were used to determine the lattice constants. Phase identification was based on the published patterns of $AgVMoO_6$ (10), MnV_2O_6 (8), $MnMoO_4$ (25), V_2MoO_8 (26), orthorhombic MoO_3 (27), hexagonal MoO_3 (28–32), V_2O_5 (33), $(Mo_xV_{1-x})O_5$ (34), and $Mn_{0.15}V_{0.3}Mo_{0.7}O_3$ (35). DTA (SETARAM M5 microanalyzer, 10°/min, Pt crucibles, samples of about 12 mg, air) and treatment of DTA curves were performed as described previously (13, 18).

3. RESULTS AND DISCUSSION

3.1. MnV_2O_6–MoO_3 Arm of the MnV_2O_6–$AgVMoO_6$–MoO_3 Diagram

This arm, including MnΦ solid solution [$0 \le X \le 42$ at room temperature or at most $X = 45$ at elevated (530°C) temperatures], has been described in (8) and reconsidered in (35). In view of the recent data a new phase $Y = Mn_{0.15}V_{0.3}M_{0.7}O_3 = Mn_{0.3}V_{0.6}Mo_{1.4}O_6$ appears at formal $X = 0.7$. Therefore, we deal with MnΦ within $0 \le X \le 42$, with MnΦ + *Y* at $42 < X < 70$, *Y* phase at $X = 70$, and Y + o-MoO_3 at $70 < X < 100$ and finally with orthorhombic MoO_3 at $X = 100$. [As mentioned in (35), due to the kinetic hindrances a pure *Y* phase has never been obtained]. The lattice constants of the *Y* phase (35) along with those belonging to the multiphasic area of the MnV_2O_6–$AgVMoO_6$–MoO_3 system (except for X–Y = 30–70) are given in Table 1. The 2θ values of the *Y* phase are almost the same for all the samples belonging to the triangle, proving that no solid solutions in the *Y* phase are formed; therefore, the average 2θ values are used for further analysis.

TABLE 1

Comparison of the Lattice Constants of the *Y* Phase, $Mn_{0.15}V_{0.3}Mo_{0.7}O_3$, in the Almost Pure State [26 Reflections, after (35)] and Average Values for Samples in the Multiphasic Area of the MnV_2O_6–$AgVMoO_6$–MoO_3 Triangle (11 Reflections, Present Paper)

Parameter	Pure *Y*	Average for the Mn–Ag–V–Mo–O field
a (Å)	11.832(2)	11.835(7)
b (Å)	3.654(1)	3.660(4)
c (Å)	10.335(3)	10.334(8)
β [deg]	101.53(2)	101.51(5)
V (Å^3)	437.8(3)	438.7(9)

Note. The *Y* phase is absent for X–Y = 30–70. For all of the remaining samples of the multiphasic area, the 2θ values of the *Y* phase are almost the same, proving that no solid solutions are formed. The average 2θ values were thus used for XRD data analysis and the average lattice constants coincide with those of the pure *Y* phase in the limit of error. Standard deviations are given in parentheses.

3.2. MnV_2O_6–$AgVMoO_6$ Arm of the MnV_2O_6–$AgVMoO_6$–MoO_3 Diagram

As will be described further in detail MnV_2O_6 and $AgVMoO_6$ are completely miscible and form MnAg solid solutions in the entire compositions range ($0 \le Y \le 100$). The XRDs data are gathered in Tables 2 and 3.

3.3. $AgVMoO_6$–MoO_3 Arm of the MnV_2O_6–$AgVMoO_6$–MoO_3 Diagram

As determined in (10) and confirmed in our laboratory AgΦ solid solutions are formed within $0 \le X \le 12$, and we deal with the coexistence of the saturated AgΦ and o-MoO_3 within $12 < X < 100$. The lattice constants of these phases are gathered in Table 4.

3.4. Range of Stability of MnAgΦ as Compared with MnNaΦ and MnLiΦ

The compositions of all the MnAgΦ samples studied are indicated in Fig., 2 (solid and open circles). X-ray phase analysis revealed that all samples of the compositions marked by solid circles give the diffraction pattern of pure brannerite, entirely indexable in a monoclinic system with

TABLE 2
Lattice Parameters of $MnAg = Mn_{1-y}Ag_yV_{2-y}Mo_yO_6$ Solid Solutions and Relative Changes $\Delta p\%$ between the End Members of the Series

Sample $X-Y$	a (Å)	b (Å)	c (Å)	β (deg)	$c \sin\beta$ (Å)	V (Å^3)
MnV_2O_6 =						
00–00	9.315(3)	3.536(1)	6.754(2)	112.66(2)	6.233(3)	205.3(2)
00–10	9.342(4)	3.549(1)	6.791(2)	112.52(2)	6.273(3)	207.0(2)
00–20	9.360(6)	3.562(1)	6.829(3)	112.41(3)	6.313(4)	210.5(3)
00–30	9.385(6)	3.572(1)	6.869(2)	112.32(1)	6.354(4)	213.0(3)
00–40	9.414(4)	3.587(1)	6.916(3)	112.29(2)	6.399(3)	216.1(3)
00–50	9.428(2)	3.603(1)	6.949(2)	112.15(1)	6.436(2)	218.6(2)
00–60	9.449(3)	3.610(1)	7.007(3)	112.02(1)	6.496(3)	221.6(2)
00–70	9.471(4)	3.621(1)	7.061(4)	111.84(2)	6.554(4)	224.8(3)
00–80	9.484(3)	3.631(1)	7.120(2)	111.50(1)	6.625(2)	228.1(2)
00–90	9.499(3)	3.647(1)	7.184(2)	111.11(1)	6.702(2)	232.2(2)
00–100	9.506(4)	3.656(1)	7.249(2)	110.71(2)	6.781(3)	235.7(3)
$= AgVMoO_6$						
$\Delta p\%$ Mn/Ag	2.05	3.39	7.33		8.79	14.79
			$NaVMoO_6$			
	9.430(4)	3.656(1)	7.257(4)	111.01(1)	6.775(4)	233.6(3)
$\Delta p\%$ Mn/Na	1.24	3.39	7.37		8.38	13.48
			$LiVMoO_6$			
	9.346(2)	3.650(1)	6.637(1)	111.65(1)	6.168(1)	210.4(1)
$\Delta p\%$ Mn/Li	0.33	3.22	−1.73		−1.04	2.50

Note. Parameters and $\Delta p\%$ values for the MnNa and MnLi series are included for comparison. Standard deviations are given in parentheses.

TABLE 4
$AgVMoO_6$–MoO_3 Arm of the Diagram: Lattice Constants of $AgVMoO_6$ (0–100), Saturated AgΦ (both marked as B), and Orthorhombic MoO_3 (o-M)

	$X-Y$							
	0–100	12–88	30–70	40–60	60–40	74–26	90–10	100–0
B								
a	9.506	9.506	9.512	9.484	9.488	9.539	t	—
b	3.656	3.659	3.658	3.657	3.658	3.663		—
c	7.249	7.225	7.217	7.205	7.211	7.247		—
β	110.71	110.48	110.47	110.37	110.41	110.67		—
V	235.66	235.41	235.27	234.18	234.55	236.99		—
o-M								
a	—	—	3.969	3.961	3.969	3.962	3.962	3.963
b	—	—	13.863	13.907	13.863	13.877	13.864	13.850
c	—	—	3.695	3.700	3.689	3.693	3.701	3.696
V	—	—	203.67	203.84	203.02	203.04	203.28	202.90

Note. Parameters a, b, c in Å, V in Å^3, β in degrees. Standard deviations are comparable to those in Tables 1 and 2. t, traces.

systematic extinctions for $h + k = 2n + 1$. The stability range of MnAgΦ thus constitutes about 40% of the MnV_2O_6–$AgVMoO_6$–MoO_3 triangle area (as compared with about 50% for MnLiΦ and about 60% for MnNaΦ, as briefly recalled in the upper part of Fig. 2). This range extends between the MnV_2O_6–$AgVMoO_6$ arm of the triangle and the S_1S_2 curve which could be approximated by two straight $(X-Y)$ segments between (45, 00), (20, 50), and (12, 88). Behind the S_1S_2 curve we deal with the multiphasic area as described in detail in Section 3.7. The stability diagram of MnAgΦ strongly resembles those for MnLiΦ (15) and MnNaΦ (18) recalled in the upper part of Fig. 2. The following features are common to all three diagrams: (i) complete miscibility of MnV_2O_6 and $LVMoO_6$,

TABLE 3
Dependence of the Lattice Parameters (p) of MnLi, MnNa, and MnAg Solid Solutions on the Composition Parameter y and the Correlation Coefficient (corr). Parameter: $p = a_0 + a_1y + a_2y^2 + a_3y^3$

Lattice parameter	Solid solution	a_0	a_1	a_2	a_3	corr
a	MnLi	$9.315 \times 10^{+00}$	3.193×10^{-04}			0.991
	MnNa	$9.313 \times 10^{+00}$	2.018×10^{-03}	-8.614×10^{-06}		0.998
	MnAg	$9.314 \times 10^{+00}$	2.663×10^{-03}	-7.027×10^{-06}		0.999
b	MnLi	$3.535 \times 10^{+00}$	1.108×10^{-03}			0.998
	MnNa/MnAg	$3.536 \times 10^{+00}$	1.338×10^{-03}	-1.398×10^{-06}		0.999
c	MnLi	$6.755 \times 10^{+00}$	-1.176×10^{-04}			0.998
	MnNa/MnAg	$6.755 \times 10^{+00}$	3.305×10^{-03}	1.636×10^{-05}		0.999
$c \sin\beta$	MnLi	$6.232 \times 10^{+00}$	-6.325×10^{-04}			0.996
	MnNa/MnAg	$6.240 \times 10^{+00}$	2.802×10^{-03}	2.444×10^{-05}		0.998
β	MnLi	$1.126 \times 10^{+02}$	-7.560×10^{-03}	-3.005×10^{-05}		0.999
	MnNa	$1.126 \times 10^{+02}$	-6.123×10^{-04}	-3.907×10^{-05}	-1.148×10^{-06}	0.995
	MnAg	$1.126 \times 10^{+02}$	-1.519×10^{-02}	2.592×10^{-04}	-3.078×10^{-06}	0.999
V	MnLi	$2.052 \times 10^{+02}$	5.103×10^{-02}			0.998
	MnNa	$2.053 \times 10^{+02}$	2.301×10^{-01}	4.700×10^{-04}		0.999
	MnAg	$2.054 \times 10^{+02}$	2.252×10^{-01}	7.574×10^{-04}		0.999

Note. $a, b, c, c \sin\beta$ in Å, V in Å^3, β in degrees.

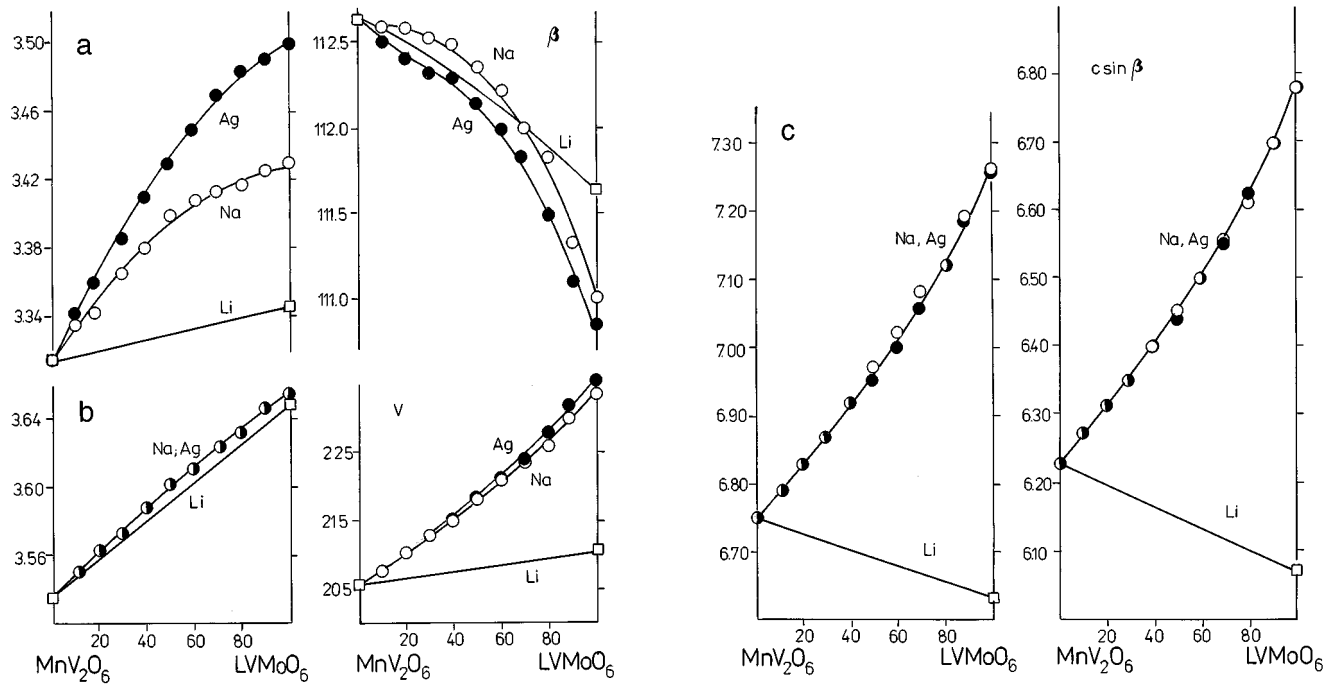

FIG. 3. Lattice parameters of MnAg, MnNa, and MnLi as a function of composition (cf. Table 1). Squares, MnLi series; open circles, MnNa series; solid circles, MnAg series; half-solid circles are common to MnNa and MnAg.

(ii) large stability area of Mn$L\Phi$ (40–60% of the triangle area), (iii) slightly concave boundary of the saturated Mn$L\Phi$ solutions. The main difference is that behind the S_1S_2 line of the saturated solid solutions we deal with the monophasic (MoO_3) area for MnLiΦ [however, in view of (35) this conclusion is to be reconsidered due to the recently discovered presence of the Y phase on the MnV_2O_6–MoO_3 arm] and with the multiphasic areas for MnNaΦ and MnAgΦ. It should be recalled here that MnV_2O_6– $AgVMoO_6$–MoO_3 is only a pseudoternary section of the MnO–Ag_2O–V_2O_5–MoO_3 system, which allows the presence of phases of composition not belonging to the triangle (15).

3.5. Lattice Parameters of MnAg as Compared with MnNa and MnLi

The determined lattice parameters of MnAg solid solutions are listed in Table 2 along with their relative changes $\Delta p\%$ between the end members of the series (p = a cell parameter $a, b, \ldots$, and $\Delta p\% = 100\Delta p/p_{y=0}$). The parameter–composition plots for MnAg compared with those for MnNa and MnLi are presented in Fig. 3. Exact comparison of the parameter–composition dependencies is crucial; therefore, the numerical, analytical data are gathered in Table 3.

There are mainly two factors influencing the lattice constants of this structure: (i) the anisotropic tightness of packing of AO_6 and BO_6 octahedra and (ii) the size (radii) of the ions. The relevant octahedral ionic radii (20, 21) are gathered in Table 5. The radii of Ag^+ taken from two references differ markedly. This problem has already been discussed in (17); the conclusion was that the radius of Ag^+ determined in (20) seems to be underestimated as compared with the remaining radii and in particular with Na^+ because of the unusual or uncertain structure of Ag_2O. It has been concluded that both radii are comparable and close to those

TABLE 5
Octahedral Ionic Radii r_6 (Å) of the Considered Ions and the Relative Changes $\Delta r\%$ between the End Members of the MnLi, MnNa, and MnAg Series of Solid Solutions

V^{5+}	Mo^{6+}	$1/2\Delta r\%$ (Mo/V)	Mn^{2+}	Li^+	$\Delta r\%$ (Li/Mn)	Na^+	$\Delta r\%$ (Na/Mn)	Ag^+	$\Delta r\%$ (Ag/Mn)	Ref.
0.465	0.498	3.5	0.823	0.728	− 11.5	1.092	32.7	0.927[a]	12.6	(20)
0.54	0.59	4.6	0.83	0.76	− 8.4	1.02	22.9	1.15	38.6	(21)

[a]In view of (17) it is rather close to 1.05 Å.

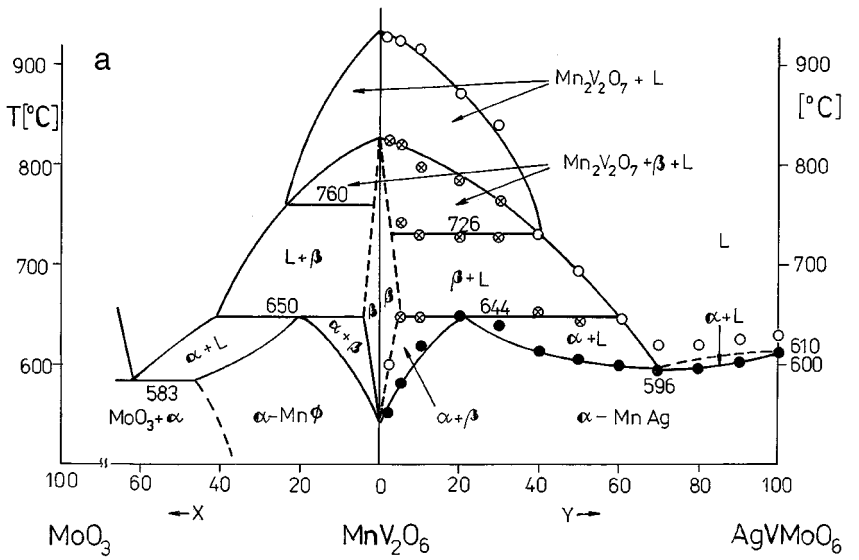
a
T[°C]
[°C]
900
800
700
600
$Mn_2V_2O_7$ + L
$Mn_2V_2O_7$ +β + L
760
726
644
650
583
596
610
L
L+β
β+L
α+L
α+β
MoO_3+α
α-Mnϕ
α – Mn Ag
100 60 40 20 0 20 40 60 80 100
X
Y
MoO_3
MnV_2O_6
$AgVMoO_6$

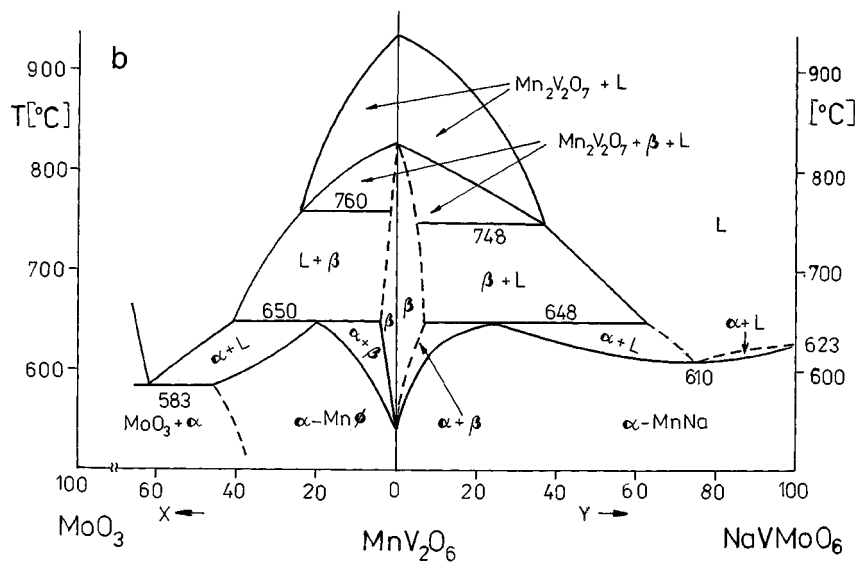
b
T[°C]
[°C]
900
800
700
600
$Mn_2V_2O_7$ + L
$Mn_2V_2O_7$ + β + L
760
748
650
648
623
610
583
L
L+β
β+L
α+L
α+β
MoO_3+α
α-Mnϕ
α-MnNa
100 60 40 20 0 20 40 60 80 100
X
Y
MoO_3
MnV_2O_6
$NaVMoO_6$

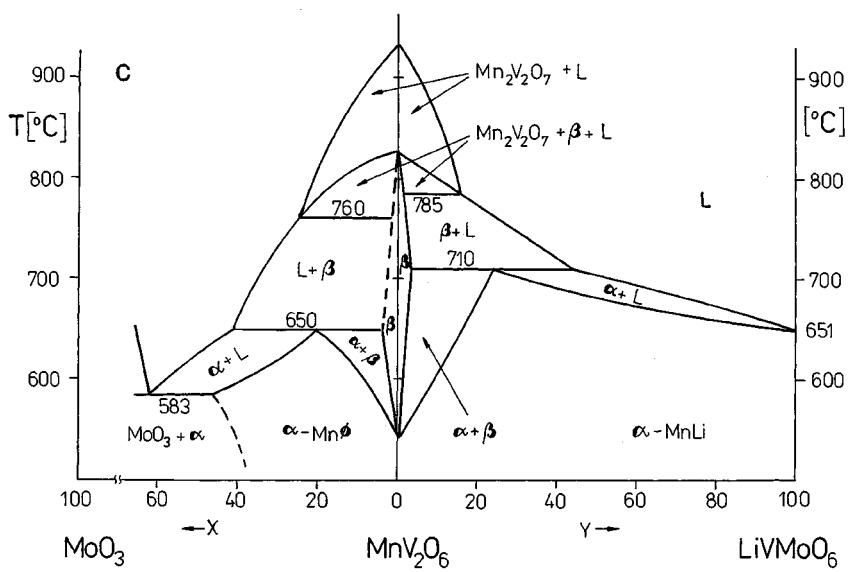
c
T[°C]
[°C]
900
800
700
600
$Mn_2V_2O_7$ + L
$Mn_2V_2O_7$ +β+ L
760
785
710
650
651
583
L
L+β
β+L
α+L
α+β
MoO_3+α
α-Mnϕ
α-MnLi
100 60 40 20 0 20 40 60 80 100
X
Y
MoO_3
MnV_2O_6
$LiVMoO_6$

in (20). Table 5 also contains the relative changes in the ionic radii $\Delta r\%$ between the end members of the MnLi, MnNa, and MnAg solid solutions considered. $\Delta r\%$ values are defined as

$$\Delta r\%(\mathrm{Ag/Mn}) = 100\,\frac{r_{\mathrm{Ag}^+} - r_{\mathrm{Mn}^{2+}}}{r_{\mathrm{Mn}^{2+}}}. \qquad [1]$$

An increase in the Y coordinate along the series of MnLi, MnNa, or MnAg solutions is equivalent to the rising extent of substitution of Mo for V (from 0 to 0.5) and Li, Na, or Ag for Mn (from 0 to 1). As the above-mentioned cations are "diluted" in the structure with oxygens of constant size, the $\Delta r\%$ values can be used only to identify the trends in changes of lattice parameters along the series of solid solutions.

The striking observation is that the linear (or almost) $b\,(Y)$ changes and the $\Delta b\%$ are nearly the same for all three series of solid solutions studied. This means that b is sensitive solely to Mo/V substitutions. Indeed, BO_6 octahedra are tight in [010] and receptive to the substitution of a bit larger Mo^{6+} for a smaller V^{5+}. On the contrary, AO_6 solids are very bulky in this direction and have enough space to accept cations even as large as Ag^+ for Mn^{2+}. However, tilting of the AO_6 [010] chains is not excluded.

As for the c and $c\sin\beta$ parameters, their values diminish along the MnLi series, which is equivalent to the narrowing distance between the BO_6 layers and due to the substitution of smaller Li^+ for the larger Mn^{2+} in AO_6 octahedra, being tight in [001]. An exactly (and strongly) opposite effect, despite the minor and nonlinear $\beta(Y)$ dependencies, is observed for MnNa and MnAg series of solutions where Na^+ and Ag^+ are more bulky as compared with Mn^{2+}. $c(Y)$ and $c\sin\beta(Y)$ overlap in the limit of error. The analytical expressions are common (Table 3). This seems to suggest again that the ionic radii of Ag^+ and Na^+ are nearly the same and equal to about 1.1 Å.

The lattice parameter a slightly increases along all three series of solid solutions studied and the slope increases in the order MnLi < MnNa < MnAg. This is surprising because the AO_6 pillars have no link in this direction. The observed fact may be ascribed to the increasing tilting of the AO_6 pillars, forcing the BO_6 layers to be more and more loose in the [100] direction. As a consequence the unit cell volume V increases in the same order, although the differences between the MnNa and MnAg series are almost negligible.

3.6. *Phase Diagram of the MnV_2O_6–$AgVMoO_6$ System as Compared with MnV_2O_6–$NaVMoO_6$ and MnV_2O_6–$LiVMoO_6$*

The phase diagram of the pseudobinary MnV_2O_6–$AgVMoO_6$ system has been determined with DTA, as shown in Fig. 4a. The temperatures of onset of endothermal effects (solid circles) and the final temperatures (open circles) have been determined accurately ($\pm 2^\circ$C). Positions of other effects, manifesting as shoulders or poorly separated peaks, were estimated tentatively (crosses). The identification of areas is based partly on the coincidence of the present diagram and that of the MoO_3–MnV_2O_6, studied previously (8) and recalled on the left side of Fig. 4a. The characteristic points of the diagram are indicated by their (Y, temperature) coordinates. It should be noted that in view of the discovery of the Y phase = $Mn_{0.3}V_{0.6}M_{1.4}O_6$ (35) at formal $X = 70$ the MoO_3–MnV_2O_6 phase diagram (8) remains valid up to $X \approx 40$ and requires revision at higher X. Correction of the rest of the diagram is intended to be done after the synthesis of the Y phase in a pure form. So far, the coincidence along the T axis above MnV_2O_6 is solely considered.

MnV_2O_6 is known (8, 15) to undergo a reversible phase transformation at Y, T (0, 540). The low-temperature α-modification crystallizes in the brannerite-type structure, while the structure of the high-temperature β-polymorph is not known [nonindexed powder X-ray pattern is given in (8)]. At (0, 825), β-MnV_2O_6 melts incongruently, decomposing to $Mn_2V_2O_7$ and liquid. The liquidus line in the MnO–V_2O_5 system over MnV_2O_6 is attained at (0, 935).

On increasing Y, i.e., on doping with $AgVMoO_6$, MnAg solid solutions are formed in both α and β matrices of MnV_2O_6. The solubility in β is at most (5, 644). There is a narrow "triangular" field of α-MnAg and β-MnAg coexistence between (0, 540), (5, 644), and (20, 644), being a simple consequence of the phase rule.

Brannerite-type α-MnV_2O_6 and $AgVMoO_6$ show miscibility in the entire composition range. Incorporation of dopant stabilizes α-MnAg against the $\alpha \rightarrow \beta$ transformation. At (20, 644), α-MnAg, revealing the highest thermal stability among the α-type solid solutions, melts incogruently,

FIG. 4. (a) Phase diagram of the pseudobinary MnV_2O_6–$AgVMoO_6$ system based on DTA and X-ray investigations. Solid circles, temperatures of onset of endothermal effects; open circles, final temperatures of endothermal effects; crosses, estimated positions of shoulders or poorly separated peaks. On the left the coincidence is shown with the previously determined (8) diagram of the MoO_3–MnV_2O_6 systems (to be corrected for $X < 40$, cf. 3.6). α and β denote low-temperature (brannerite) and high-temperature polymorphs of MnAg, respectively; L, liquid. (b) Previously determined (16) phase diagram of the MnV_2O_6–$NaVMoO_6$ system. (c) Previously determined (15) phase diagram of the MnV_2O_6–$LiVMoO_6$ system.

decomposing to β-MnAg and liquid, represented by (5, 644) and (60, 644), respectively. On heating the samples of $5 < Y < 40$ above 644°C, and before total melting, one crosses the areas of coexistence of $Mn_2V_2O_7$ + β-MnAg + liquid and $Mn_2V_2O_7$ + liquid. On heating the samples of $40 < Y < 60$, one directly crosses the liquidus. In the range of $20 < Y \leq 100$ and $610 < T < 644$, there are two areas of coexistence of α-MnAg + liquid with a shallow minimum of solidus–liquidus at (70, 596).

The previously determined (16) phase diagram of the MnV_2O_6–$NaVMoO_6$ system, recalled in Fig. 4b, has exactly the same shape; even the characteristic points of the diagram almost overlap, which remains analogous to the X-ray pictures of both systems. Figure 4c recalls the phase diagram of the MnV_2O_6–$LiVMoO_6$ system (15), which is highly analogous to both formerly described. There are two minor differences: (i) the areas involving $Mn_2V_2O_7$ are smaller, (ii) a minimum solidus line at about $Y = 70$ does not exist for MnLi because the ΔT between the peritectic temperature and melting point of $LiVMoO_6$ is much higher as compared with both remaining systems.

3.7. *Multiphasic Area of the $Mn_2V_2O_6$–$AgVMoO_6$–MoO_3 Diagram*

Table 6 contains the lattice parameters of the almost saturated MnAgΦ solid solutions. In accord with MnAg the lattice parameters increase systematically with Y, which again is a consequence of the larger ionic radii of the dopants as compared with the mother cations.

As shown in Tables 7 and 8, behind the S_1S_2 curve we deal with the multiphasic area in which the saturated brannerite-type (B) phases coexist almost everywhere with the Ag–Mn-stabilized hexagonal MoO_3 (h-M) (to be commented on below), $Y = Mn_{0.15}V_{0.3}Mo_{0.7}O_6$ and $(Mo_xV_{1-x})O_3$ (VM), and sometimes with orthorhombic MoO_3 (o-M) and $MnMoO_4$ (MM); the XRD reflections of the latter usually overlap with those of other phases which makes it impossible to determine the lattice parameters. As already mentioned the lattice constants of Y are gathered in Table 1 and those of the remaining phases are given in Table 8.

TABLE 6
Lattice Parameters for the Almost Saturated $MnAg\Phi = Mn_{1-x-y}Ag_y\Phi_xV_{2-2x-y}Mo_{2x+y}O_6$ Solid Solutions

	X–Y								
	40–00	35–10	30–20	30–30	20–40	20–50	20–60	10–80	12–88
a	9.378	9.411	9.415	9.468	9.481	9.444	9.490	9.513	9.506
b	3.613	3.617	3.617	3.631	3.626	6.633	3.644	3.654	3.659
c	6.751	6.821	6.850	6.905	6.950	7.004	7.070	7.169	7.225
β	112.18	112.08	112.06	111.90	111.92	111.51	111.25	110.98	110.48
V	211.8	215.1	216.2	220.2	221.6	223.6	227.9	232.7	235.4

Note. Parameters a, b, c are given in Å, V in Å^3, β in degrees; standard deviations are at most 3 at the last decimal indicated.

TABLE 7
Lattice Parameters of the Mn–Ag-Stabilized Hexagonal MoO_3

Sample X–Y	a (Å)	c (Å)	V (Å^3)
30–60	9.863(14)	11.000(12)	927(4)
40–30	9.864(08)	10.929(09)	920(2)
50–10	9.860(03)	10.951(05)	922(1)
50–40	9.914(12)	10.886(18)	927(4)
60–10	9.864(08)	10.963(12)	924(3)
60–20	9.886(11)	10.957(11)	927(3)
70–10	9.839(07)	10.920(18)	915(3)
70–20	9.885(19)	11.012(19)	932(5)
80–10	9.867(07)	10.955(06)	924(2)
Average	9.871(10)	10.953(12)	924(3)

Note. Standard deviations in parentheses.

In view of identifying the presence of the Ag-containing h-MoO_3 it seems relevant to recall the following. h-MoO_3 belongs to the family of defective phases containing dopants (29–31, 33). In all these structures the hexagonal molybdate framework (partly doped with V) consists of zig-zag chains of edge-shared octahedra parallel to the c axis; these chains share corners to create large [001] tunnels which are suited to accommodate large alkali metals (L = K, Rb, Cs, or ammonium, alone or hydrated), which in turn stabilize a series of isomorphous compounds. According to the quoted literature the range of possible changes in composition is very narrow and in practice (a dry) h-MoO = $L_{0.13}(V_{0.13}Mo_{0.87})O_3$ (=Q; L = monovalent element). The dimensions of their unit cells (dry phases) depend slightly on the chemical composition. For L = K, i.e., for h-MoO_3(K), they are $a = 10.481$ Å, $c = 3.701$ Å, and $V = 352.1$ Å^3. The doubled Q formula belongs to our MeV_2O_6–$LVMoO_6$–MoO_3 triangle with coordinates X–Y = 76–24. h-MoO_3 with L = Ag has never been mentioned in the literature; Ag was believed to be too small to stabilize the peculiar h-MoO_3 structure. Indeed, along the $AgVMoO_6$–MoO_3 axis of the system and beside X–Y = 12–88 we deal with mixtures of saturated AgΦ and orthorhombic MoO_3. However, inside the MnV_2O_6–$AgVMoO_6$–MoO_3 triangle we doubtless deal with the h-MoO_3 phase, apparently stabilized by both Ag and Mn, i.e., h-MoO_3 (Ag, Mn), as summarized in Table 7. The lattice constants of h-MoO_3 (Ag, Mn) are on average $a = 9.871$ Å and $c = 10.953$ Å with $V = 942$ Å^3. It is not strange that a is a bit smaller as compared with h-MoO_3(K) because the ionic radii of Ag^+ and Mn^{2+} are smaller as compared with that of K^+. The parameter c corresponding to the direction of the [001] tunnels is three times higher for h-MoO_3(Ag, Mn) as compared with

TABLE 8
Lattice Constants of Compounds Present in the *X–Y* Samples Belonging to the Multiphasic Area of the MnV_2O_6–$AgVMoO_6$–MoO_3 Triangle

Phase		Pure Mn–B	30–60	40–30	50–10	50–40	60–10	60–20	70–10	70–20	75–20	80–10	Pure Ag–B
B	*a*	9.315	9.50	9.43	9.41	9.49	9.41	9.35	9.40	9.39	?	9.36	9.506
	b	3.546	3.65	3.63	3.63	3.66	3.63	3.63	3.63	3.61		3.61	3.656
	c	6.754	7.14	6.90	6.82	7.04	6.84	6.92	6.84	6.95		6.92	7.249
	β	112.66	110.9	111.8	112.0	110.9	112.1	112.8	111.8	112.9		112.9	110.71
	V	205.3	231.5	219.0	215.8	228.7	216.5	216.2	216.8	217.1		215.3	235.66
		V_2O_5											
VM	*a*	11.519	11.75	11.54	11.50	11.69	11.49	11.59	11.54	11.54	11.53	11.58	—
	b	3.563	3.66	3.57	3.57	3.57	3.57	3.56	3.58	3.54	3.54	3.56	
	c	4.373	4.40	4.34	4.33	4.39	4.34	4.34	4.35	4.35	4.38	4.37	
	V	179.2	187.1	178.8	178.8	183.0	177.8	178.9	179.5	178.4	181.1	179.2	
		MoO_3											MoO_3
o-M	*a*	3.963	—	—	—	—	—	—	3.96	3.97	3.97	3.97	3.963
	b	13.855							13.87	13.86	13.87	13.87	13.855
	c	3.696							3.69	3.69	3.69	3.69	3.696
	V	202.9							202.7	203.1	203.2	203.2	202.9
MM		—	?	?	+	+	?	+	+	—	—	—	—
h-Mo		See Table 7											
Y		See Table 1											

Note. *B* = brannerite, VM = $(Mo_xV_{1-x})O_5$, o-M = orthorhombic MoO_3, MM = $MnMoO_4$, Mn–B = MnV_2O_6, Ag–B = $AgVMoO_6$. Parameters *a*, *b*, *c* are given in Å, *V* in Å^3, and *β* in the degrees and are rounded according to the worst standard deviation in each set. +, present; —, absent; ?, perhaps present. Parameters for the almost saturated MnΦ (*X–Y* = 40–00) and AgΦ (*X–Y* = 12–88) are given in Table 6.

h-MoO_3(K), which may be ascribed either to the presence of two dopants or to minor changes in the $(MoO_x)_n$ host lattice. Further attempts to obtain a pure h-MoO_3(Ag, Mn) are necessary.

4. CONCLUSIONS

MnV_2O_6 of the brannerite-type structure (below 540°C), referred to as α, doped with MoO_3 and Ag_2O forms isomorphous solid solutions $MnAg\Phi = Mn_{1-x-y}Ag_y\Phi_xV_{2-2x-y}Mo_{2x+y}O_6$ (Φ, cation vacancy in the original Mn position). They belong to the pseudoternary MnV_2O_6–$AgVMoO_6$–MoO_3 system which may be visualized as an equilateral triangle with coordinates $X = 100x$ and $Y = 100y$ marked along its MnV_2O_6–MoO_3 and MnV_2O_6–$AgVMoO_6$ arms, respectively. The particular cases are $MnAg = Mn_{1-y}Ag_yV_{2-y}Mo_yO_6$ $(x = 0)$, $Mn\Phi = Mn_{1-x}\Phi_xV_{2-2x}Mo_{2x}O_6$ $(y = 0)$, and $Ag\Phi = Ag_{1-x}\Phi_xV_{1-x}Mo_{1+x}O_6$ $(x + y = 1)$. MnV_2O_6 and $AgVMoO_6$ show miscibility in the entire composition range (MnAg). The opposite boundary of the MnAgΦ phases, S_1S_2, passes through the X, Y points (45, 00), (20, 50), and (12, 88). As the ionic radii of dopants (Ag^+/Mn^{2+}, Mo^{6+}/V^{5+}) are larger than those of the mother cations the lattice constants of both MnAg and almost saturated MnAgΦ (along S_1S_2) rise systematically with *Y*. Behind the S_1S_2 boundary we deal with the saturated MnAgΦ accompanied by Ag–Mn-stabilized hexagonal MoO_3, the *Y*-phase $Mn_{0.15}V_{0.3}Mo_{0.7}O_3$, and $(Mo_xV_{1-x})O_5$, and in some areas by $MnMoO_4$ and orthorhombic MoO_3. The relation between the *L* size and the stability of Mn*L*Φ is not clear at present. From the determined phase diagram of the pseudobinary MnV_2O_6–$AgVMoO_6$ system, the limit of thermal stability of α-MnAg extends between the *Y*, *T* points (0, 540), (20, 644), (70, 596), and (100, 610). The phase diagram shows (i) a narrow double-lens-type solidus–liquidus gap at high values of *Y*, with a shallow minimum at *Y*, $T = (70, 596)$; (ii) two peritectic meltings at lower *Y* (yielding the high-temperature *β*-MnAg polymorph at 644°C and $Mn_2V_2O_7$ at 726°C); and (iii) a small area of *β*-MnAg within $540 < T < 825$ with $Y_{max} \approx 5$ at 644°C. Close analogy of this diagram with those of MnV_2O_6–$LiVMoO_6$ and MnV_2O_6–$NaVMoO_6$ has been observed.

REFERENCES

1. R. Ruh and A. D. Wadsley, *Acta Crystallogr.* **21,** 974 (1996).
2. J. Angenault and A. Rimsky, *C.R. Acad. Sci. Paris* **267,** 227 (1968).

3. J. C. Buloux and J. Galy, *Bull. Soc. Chim. Fr.* **3,** 736 (1969).
4. J. Angenault, *Rev. Chim. Miner.* **7,** 651 (1970).
5. H. N. Nag and C. Calvo, *Canad. J. Chem.* **50,** 3619 (1972).
6. E. E. Sauerbrei, M.Sc. thesis, McMaster University, Ontario, Canada, 1972.
7. C. Calvo and D. Manolescu, *Acta Crystallogr. Sect. B* **29,** 1743 (1973).
8. R. Kozłowski, J. Ziółkowski, K. Mocała, and J. Haber, *J. Solid State Chem.* **35,** 1 (1980); erratum **38,** 138 (1981).
9. K. Mocała and J. Ziółkowski, *J. Solid State Chem.* **69,** 299 (1987) and quotations.
10. J. Galy, J. Darriet, and B. Darriet, *C.R. Acad. Sci. Paris Ser. C* **264,** 1477 (1967).
11. B. Darriet and J. Galy, *Bull. Soc. Fr. Mineral. Cristallogr.* **91,** 325 (1968).
12. B. Darriet and J. Galy, *C.R. Acad. Sci. Paris. Ser. C* **266,** 1698 (1968); JCPDS 21-710.
13. K. Mocała, J. Ziółkowski, and L. Dziembaj, *J. Solid State Chem.* **56,** 84 (1985).
14. K. Mocała and J. Ziółkowski, *J. Solid State Chem.* **71,** 426 (1987).
15. J. Ziółkowski, K. Krupa, and K. Mocała, *J. Solid State Chem.* **48,** 376 (1983).
16. B. Masłowska and J. Ziółkowski, *J. Solid State Chem.* **110,** 74 (1994).
17. K. Mocała and J. Ziółkowski, *J. Solid State Chem.* **71,** 522 (1987).
18. B. Masłowska and J. Ziółkowski, *J. Solid State Chem.* **87,** 208 (1990).
19. T. Machej, R. Kozłowski, and J. Ziółkowski, *J. Solid State Chem.* **38,** 97 (1981).
20. J. Ziółkowski, *J. Solid State Chem.* **57,** 269 (1985).
21. R. D. Shannon, *Acta Crystallogr. Sect. A* **32,** 751 (1976).
22. J. Ziółkowski and L. Dziembaj, *J. Solid State Chem.* **57,** 291 (1985).
23. B. Napruszewska, P. Olszewski, and J. Ziółkowski, in preparation.
24. P. Courty, H. Ajot, and C. Marcilly, *Powder Technol.* **7,** 21 (1973).
25. S. C. Abrahams and J. M. Reddy, *J. Chem. Phys.* **43,** 2533 (1965).
26. M. A. Eick and L. Kihlborg, *Acta Chim. Scand.* **20,** 1659 (1966).
27. JCPDS 9-387.
28. JCPDS 21-569.
29. B. Darriet and J. Galy, *J. Solid State Chem.* **8,** 189 (1973).
30. Y. Hu and P. K. Davies, *J. Solid State Chem.* **105,** 489 (1993).
31. Y. Hu and P. K. Davies, *J. Solid State Chem.* **119,** 176 (1995).
32. N. A. Caiger, S. Crouch-Baker, P. G. Dickens, and G. S. James, *J. Solid State Chem.* **67,** 369 (1987).
33. H. G. Bachman, F. R. Ahmed, and W. H. Barnes, *Z. Kristallogr.* **115,** 110 (1961).
34. F. Y. Robb, W. S. Glaunsinger, and P. Courtine, *J. Solid State Chem.* **30,** 171 (1979).
35. J. Ziółkowski, P. Olszewski, and B. Masłowska-Napruszewska, submitted for publication.